Correlation of Measured Induced Velocities with a Finite-State Wake Model

David A. Peters
Professor

Cheng Jian He
Post-Doctoral Fellow

School of Aerospace Engineering
Georgia Institute of Technology
Atlanta, Ga.

A new rotor induced-flow model is applied to the correlation of a recent set of LDV inflow measurements made by the Army Labs at NASA Langley. This new inflow model is based on an acceleration potential with a skewed cylindrical wake. While this particular flow description is not new, the novel aspect of the present work is that the model is not discretized. Instead, the flow field and the rotor lift are expanded in terms of appropriate inflow modes. The result is a set of closed-form, first-order, ordinary differential equations in time that defines a finite number of modal inflow states, with blade lift as the forcing function. Although the model is intended primarily as a representation of unsteady aerodynamics for aeroelasticity applications, the results here show that it is also effective as a means of finding the inflow distribution in forward flight.

Notation

a = slope of lift coefficient curve, 1/rad
$\bar{c}$ = nondimensional blade chord
$\overline{C_T}$ = steady value of thrust coefficient
C_n^m, D_n^m = arbitrary pressure coefficients
$E[\ ]$ = dynamic inflow acceleration operator
G_n^m = diagnonal mass matrix
H_n^m = factorial ratios, Eq. (26)
i = imaginary number, $i = \sqrt{-1}$
j = polynomial number
$L[\ ]$ = quasi-steady inflow operator
$[\bar{L}_{jn}^{rm}]^c$ = cosine influence coefficients
$[\bar{L}_{jn}^{rm}]^s$ = sine influence coefficients
L_q = blade sectional lift of q^{th} blade, N/m
m = harmonic number
M = total number of harmonics
n = polynomial number
P = pressure across disk divided by $\rho\Omega^2R^2$
$\overline{P}_n^m$ = normalized Legendre function of first kind
P_n^m, Q_n^m = associated Legendre function of first and second kinds
Q = number of blades
q = blade index
q_i = i-th component of perturbation velocity, dimensionless on ΩR
R = rotor radius, m
r = harmonic number
$\bar{r}$ = nondimensional blade radial coordinate
S = total inflow states
t = time, sec
$\bar{t}$ = nondimensional time, $\bar{t} = \Omega t$
V = flow parameter, dimensionless on ΩR
V_T = total flow at rotor plane divided by ΩR
V_∞ = nondimensional freestream speed
w = nondimensional normal component of induced velocity, positive downward
X = function of wake skew angle, $X = \tan|\chi/2|$
α = angle between freestream and rotor disk, positive nose down
α_j^r, β_j^r = induced inflow expansion coefficients
$\overline{\alpha}_1^0$ = steady value of α_1^0
χ = wake skew angle, $\pi/2 - \tan^{-1}|\lambda/\mu|$
θ_q = pitch angle of q^{th} blade, rad
θ_0 = blade collective pitch at blade root, rad
θ_t = blade linear twist, rad
θ_{1c} = blade lateral cyclic pitch, rad
θ_{1s} = blade longitudinal cyclic pitch, rad
λ = total mass-flow inflow, $\lambda = \lambda_f + \lambda_{in}$

Presented at the 45th Annual National Forum of the American Helicopter Society, Boston, Mass., May 1989

λ_f = inflow due to freestream, $V_\infty \sin(\alpha)$
λ_m = momentum theory inflow, Eq. (35)
μ = advance ratio, $V_\infty \cos(\alpha)$
$\nu, \eta, \bar{\psi}$ = ellipsoidal coordinates, dimensionless
ξ = nondimensional coordinate along freestream line, positive upstream
ρ = air density, kg/m^3
$(\rho_n^m)^2$ = integral (0 to 1) of $(P_n^m(\nu))^2$
σ = rotor solidity
τ_n^{mc} = cosine pressure coefficient
τ_n^{ms} = sine pressure coefficient
$\bar{\tau}_1^{0c}$ = steady part of τ_1^{0c}
$\phi_n^m(\bar{r})$ = inflow expansion functions, $\bar{P}_n^m(\nu)/\nu$
Φ = nondimensional pressure
ψ = spacial position at rotor disk
ψ_q = azimuth of q^{th} blade
Ω = rotor rotational speed, rad/sec
$(\,)^*$ = derivative with respect to nondimensional time, $(\,)^* = \partial/\partial\bar{t}$
$(n)!!$ = double factorial of n,
= $(n)\,(n-2)\,(n-4)\cdots(2)$, for n even;
= $(n)\,(n-2)\,(n-4)\cdots(1)$, for n odd

Introduction

Background

The task of aeroelastic analysis of a rotorcraft involves several key elements. First, appropriate models must be obtained for the various components of the problem. These include a lift model (quasi-steady, dynamic stall, panel code, etc.), an induced-flow model (momentum-theory, Glauert, Drees, prescribed wake, free wake, etc.), a blade model (rigid-blade, linear beam, Hodges-Dowell, etc.), a fuselage model (rigid-body, NASTRAN, etc.), and possibly a feedback control model (stabilizer bar, SCAS, higher-harmonic control, etc.). Second, these models must be coupled together and solved simultaneously to find a trimmed, periodic equilibrium condition. This second task is not at all trivial and is often compounded by the fact that the aerodynamic, structural, and control-system models are often mutually incompatible both in terms of connecting variables and in terms of available solution strategies.

Finally, the trimmed periodic solution to this coupled system must be perturbed (analytically or numerically) in order to obtain a set of linearized, periodic-coefficient equations that can be analyzed for Floquet stability, for frequency and damping, and for the design of active control systems. This third (and crucial) step is often hindered due to the fact that lift or inflow models do not have finite number of state variables that can be identified and perturbed. Instead, these models often contain hidden states (or sometimes an infinite number of states), which precludes efficient aeroelastic analysis and iterative design. What we need are lift and inflow models that are accurate and that are expressive in terms of a reasonable number of state variables. This paper develops a theory and presents applications of such a finite-state inflow model.

Previous Work

At this point, it is instructive to review the various unsteady inflow models that are available to aeroelasticians in the rotary-wing field. One of the best-known models is Loewy theory, Ref. 1. It provides induced velocity in axial flight due to shed vorticity including the returning wake. It is written as a two-dimensional lift-deficiency function that explicitly includes the Theodorsen function. Thus, it is in the frequency domain and has an infinite number of states. Friedmann and Venkatesan, Ref. 2, offer a methodology whereby Loewy theory can be approximated by a finite number of states in the time domain. Still, however, the number of states is large (17 variables at each radial lift element on each blade). Furthermore, the Loewy methodology does not treat induced flow due to trailing vorticity and is not applicable in forward flight. Thus, the finite-state approximation is also limited to hover or climb without trailing vorticity.

Other pertinent methods include actuator-disk theories that assume a skewed cylindrical wake in forward flight, Refs. 3–5. These include both acceleration-potential and vortex-cylinder methods. They are related to our present method, but they are inadequate in that they are steady-state models that must assume an infinite number of blades in order to obtain closed-form performance results. Thus, they are not unsteady, three-dimensional wake models. One alternative model that captures both the unsteady and the three-dimensional aspects of rotor induced flow is that of Miller, Ref. 6. Although the model has some very useful applications (as well as interesting special cases), its solution is in the frequency domain and requires integrals over the wake that can become involved. It also has an infinite number of states and cannot be applied in the aeroelasticity context described in this paper.

Another important class of models is in the set of vortex-filament models, which have dominated performance calculations over the past 20 years (*e.g.*, Refs. 7–9). Some of these have only trailing vorticity (with the shed wake accounted for by Loewy or Theodorsen functions), but others have both shed and trailing filaments. When the wake is prescribed, influence coefficients can be calculated between the strength of vortex filaments and the induced flow at the rotor. The result is a fairly efficient induced flow methodology that is both unsteady and three-dimensional. While these methods are very powerful tools for rotor performance, they still do not meet the needs for aeroelasticity analysis. First, the discretization process, which is adequate for loads, often falls short for unsteady perturbations. There are four major discretizations involved. The first is the spanwise discretization of vortex filaments, the second is the piece-wise discretization of bound vortices, the third is the accompanying discretization of shed filaments (often every 15° of rotor azimuth), and the fourth is the truncation of the wake after a few turns. These discretizations are generally much less accurate for aeroelasticity than they are for performance.

An even more serious problem, however, is that a discretized wake does not have well-defined states and is not easily perturbed. Thus, with conventional dynamic perturbations, one either must freeze the wake (in which case unsteady aerodynamics is lost) or else allow the wake to be implicitly perturbed along with structural states (which contaminates the perturbation dynamics with the dynamics of hidden inflow states). Therefore, vortex filament methods do not satisfy our requirements; and there is a need for a different kind of three-dimensional, unsteady wake model.

Present Approach

The inflow description of this paper is a three-dimensional, unsteady induced-flow model with a finite number of states in the time domain. The basis of the model is an acceleration potential with a skewed cylindrical wake. Thus, its roots are in Refs. 3–5. However, unlike those methods, this model is both unsteady and is applicable to a finite number of blades. Models with a similar basis have been used in rotary-wing work, Ref. 10; but the unique aspect here is the solution methodology. Rather than discretize the wake and couple it to a given blade model, we expand the induced inflow at the disk in terms of modal functions. The blade lift is also expressed as an expression on the disk and is left general. The result is a set of ordinary differential equations (in closed form) that

relate the expansion coefficients of inflow to the expansion coefficients of arbitrary lift. The inflow expansion coefficients thus become states of the model, and the forcing terms can be derived based on any lifting theory (linear or nonlinear).

The theory of dynamic inflow, Ref. 11, can be thought of as a special case of this theory but with only 3 inflow expansion terms (uniform, side-to-side gradient, and fore-to-aft gradient). Furthermore, Ref. 12 (in which the foundations of this new theory are set forth) shows that the new model implicitly includes Theodorsen and Loewy effects (from the shed wake) as well as Prandtl-Goldstein tip losses (due to the trailing wake). Thus, the method is truly an unsteady, three-dimensional wake model with a finite number of states. The method is not expected to replace vortex-filament theories for performance work due to the lack of wake distortion or wake roll-up in the model. Still, the present method should be capable of predicting reasonable unsteady induced-flow distributions in forward flight in order to provide a valid trim state about which to perturb. Therefore, in this paper, we concentrate on correlations of the theory with induced-flow measurements in forward flight.

Formulation of Theory

Fluid Mechanics

For an incompressible potential flow with small perturbations, the continuity and momentum equations can be written in index notation as

$$q_{i,i} = 0 \tag{1}$$

$$\overset{*}{q}_i - V_\infty q_{i,\xi} = -\Phi_{,i} \tag{2}$$

where q_i are the velocity components, Φ is the pressure, $(\ )^*$ is a nondimensional time derivative, and $(\ )_{,\xi}$ is the derivative along the freestream line.

From Eq. (2), it can be seen that spatial gradient of the pressure is a superposition of contributions from both the unsteady rate of change in velocity and the gradient of velocity along the freestream direction. This suggest a division of the pressure into two parts (*i.e.*, the part due to momentum flux, denoted as Φ^V, and the part due to acceleration, noted as Φ^A). Then the pressure can be expressed as

$$\Phi = \Phi^V + \Phi^A \tag{3}$$

$$\Phi_{,i} = \Phi^V_{,i} + \Phi^A_{,i} \tag{4}$$

$$\Phi^V_{,i} = V_\infty q_{i,\xi} \tag{5}$$

$$\Phi^A_{,i} = -\overset{*}{q}_i \tag{6}$$

If we differentiate Eqs. (5) and (6) with respect to the index i and use the continuity equation, Eq. (1), a Laplace's equation can be obtained for each pressure function as follows,

$$\Phi^V_{,ii} = 0; \qquad \Phi^A_{,ii} = 0 \tag{7}$$

Equation (7) indicates that each part of the total pressure satisfies Laplace's equation. Thus, Φ can be represented as an acceleration potential.

When Laplace's equation is written in ellipsoidal coordinates, it can be solved analytically by the method of separation of variables. The potential functions thus obtained can be combined to given an arbitrary pressure discontinuity across a circular disk, Ref. 3. When the condition of a bounded solution is invoked, the general form of the acceleration potential becomes

$$\Phi = \sum_m^\infty \sum_{n=m+1,m+3,\ldots}^\infty P_n^m(\nu) Q_n^m(i\eta)[C_n^m(\bar{t})\cos(m\bar{\psi}) + D_n^m(\bar{t})\sin(m\bar{\psi})] \tag{8}$$

where $P_n^m(\nu)$ and $Q_n^m(i\eta)$ are associated Legendre functions of the first and second kind, respectively; C_n^m and D_n^m are arbitrary, time-dependent coefficients; and ν, η, and $\bar{\psi}$ are ellipsoidal coordinates as described in Ref. 11.

It is important to note that, since ν is positive above the disk and negative below the disk, the functions $P_n^m(\nu)$ with $n + m$ odd yield a discontinuity in pressure across the disc at which $\eta = 0$, $\nu = \sqrt{1 - \bar{r}^2}$, and $\bar{\psi} = \psi$. Therefore, rotor lift can be obtained from the pressure difference between the upper and lower surfaces of the disk,

$$P = \sum_{m,n}^\infty \bar{P}_n^m(\nu)[\tau_n^{mc}(\bar{t})\cos(m\psi) + \tau_n^{ms}(\bar{t})\sin(m\psi)] \tag{9}$$

where

$$\bar{P}_n^m(\nu) = (-1)^m \frac{P_n^m(\nu)}{\rho_n^m} \tag{10}$$

$$(\rho_n^m)^2 = \frac{1}{(2n+1)} \frac{(n+m)!}{(n-m)!} \tag{11}$$

$$\tau_n^{mc} = (-1)^{m+1} 2 Q_n^m(i0) \rho_n^m C_n^m \tag{12}$$

$$\tau_n^{ms} = (-1)^{m+1} 2 Q_n^m(i0) \rho_n^m D_n^m \tag{13}$$

Operator Notation

To establish a relation between the induced flow of a lifting rotor and the blade loads, let us start with Eqs. (5) and (6). Integration of Eq. (5) along the freestream direction results in

$$q_i = -\frac{1}{V_\infty} \int_\xi^\infty \Phi^V_{,i}\, d\xi \tag{14}$$

Then, from Eq. (6), we have

$$\overset{*}{q}_i = -\Phi^A_{,i} \tag{15}$$

Now, if we are only interested in the normal component of induced inflow at the rotor disk, Eqs. (14) and (15) can be placed in the following forms.

$$w = -\frac{1}{V_\infty} \int_0^\infty \frac{\partial \Phi^V}{\partial z}\, d\xi \tag{16}$$

$$\frac{dw}{d\bar{t}} = -\frac{\partial \Phi^A}{\partial z}\Big|_{\eta=0} \tag{17}$$

Equations (16) and (17) can be thought of as linear operators,

$$w = L[\Phi^V] \tag{18}$$

$$\overset{*}{w} = \frac{dw}{d\bar{t}} = E[\Phi^A] \tag{19}$$

At this stage, we assume that the operators L and E are invertable, and then we obtain an equation for inflow in the following form

$$E^{-1}[w]^* + L^{-1}[w] = \Phi^A + \Phi^V = \Phi \tag{20}$$

If we choose a proper series expansion for induced flow, each of the operators L and E can be expressed in a matrix form, which allows a matrix inversion.

Analogous to the expansion of pressure, the induced flow can be represented in terms of azimuthal harmonics and radial distribution functions. The best choice for the radial expansion has been found to be

$$w(\bar{r}, \psi, \bar{t}) = \sum_{r,j}^{\infty} \phi_j^r(\bar{r})[\alpha_j^r(\bar{t})\cos(r\psi) + \beta_j^r(\bar{t})\sin(r\psi)] \quad (21)$$

where $\phi_n^m(\bar{r}) = \bar{P}_n^m(\nu)/\nu$ and $\nu = \sqrt{1 - \bar{r}^2}$. Interestingly, the $\phi_n^m(\bar{r})$ are simple polynomials in the radial position, $\bar{r}$, and have only even (or odd) powers of $\bar{r}$ ranging from m to $n - 1$.

$$\phi_n^m(\bar{r}) = \sqrt{(2n + 1)H_n^m} \sum_{q=m,m+2,\cdots}^{n-1} \bar{r}^q(-1)^{(q-m)/2} \frac{(n + q)!!}{(q - m)!!(q + m)!!(n - q - 1)!!} \quad (22)$$

With pressure and velocity each represented by the above expansions, the operators in Eq. (20) can be expressed as square matrices that relate the pressure coefficients (τ_n^{mc}, τ_n^{ms}) to the velocity coefficients (α_j^r, β_j^r) (for details, see Ref. 13). Thus, Eq. (20) takes the form

$$[\nwarrow G_n^m \searrow]\{\alpha_j^r\}^* + 2V[\bar{L}^c]^{-1}\{\alpha_j^r\} = \{\tau_n^{mc}\} \quad (23)$$

$$[\nwarrow G_n^m \searrow]\{\beta_j^r\}^* + 2V[\bar{L}^s]^{-1}\{\beta_j^r\} = \{\tau_n^{ms}\} \quad (24)$$

where G_n^m results from Eq. (17) and is given by

$$G_n^m = \frac{4}{\pi} H_n^m \quad (25)$$

$$H_n^m \equiv \frac{(n + m - 1)!!(n - m - 1)!!}{(n + m)!!(n - m)!!} \quad (26)$$

and where $\bar{L}^c$ and $\bar{L}^s$ arise from Eq. (16) and depend on the wake skew angle χ ($\chi = 0°$ in axial flow through $\chi = 90°$ in pure-edgewise flow).

$$[\bar{L}_{jn}^{0m}]^c = (X^m)[\Gamma_{jn}^{0m}] \quad (27)$$

$$[\bar{L}_{jn}^{rm}]^c = (X^{|m-r|} + (-1)^l X^{|m+r|})[\Gamma_{jn}^{rm}] \quad (28)$$

$$[\bar{L}_{jn}^{rm}]^s = (X^{|m-r|} - (-1)^l X^{|m+r|})[\Gamma_{jn}^{rm}] \quad (29)$$

where $l = \min(r, m)$, and $X = \tan|\chi/2|$. Note that $0 \le X \le 1$. All sine and cosine elements depend on the same coefficients Γ_{jn}^{rm} that can be found in closed-form as follows.

$$\Gamma_{jn}^{rm} = \frac{(-1)^{(n+j-2r)/2}}{\sqrt{H_n^m H_j^r}} \frac{2\sqrt{(2n + 1)(2j + 1)}}{(j + n)(j + n + 2)[(j - n)^2 - 1]} \quad \text{for } r + m \text{ even} \quad (30)$$

$$\Gamma_{jn}^{rm} = \frac{\pi}{2\sqrt{H_n^m H_j^r}} \frac{\text{sgn}(r - m)}{\sqrt{(2n + 1)(2j + 1)}} \quad \text{for } r + m \text{ odd}, j = n \pm 1 \quad (31)$$

$$\Gamma_{jn}^{rm} = 0 \quad \text{for } r + m \text{ odd}, j \ne n \pm 1 \quad (32)$$

$\bar{L}$ is partitioned such that the superscripts are row-column indices of the r, m partition, and the subscripts (j, n) are the row-column indices of the elements within each partition. We must note, however, that these indices do not take the traditional matrix values of $1, 2, 3, \cdots$. Instead, for the cosine equation, $m = 0, 1, 2, 3, \cdots$; for the sine equation, $m = 1, 2, 3, \cdots$; and for either set, $n = m + 1, m + 3, m + 5, \cdots$ (r and j follow the same convention).

As a further extension of the theory, we have replaced V_x with an equivalent V to account for energy added to the flow from the rotor

$$V = \frac{\mu^2 + (\lambda + \lambda_m)\lambda}{\sqrt{\mu^2 + \lambda^2}} \quad (33)$$

$$\lambda = \lambda_m + \lambda_f \quad (34)$$

where V comes from momentum considerations, Ref. 11; μ and λ_f are the inplane and normal components of V_x; and λ_m is the momentum-theory value of steady induced flow for a trimmed rotor,

$$\lambda_m = \frac{1}{2}\frac{\bar{C}_T}{V_T} \cong \sqrt{3}\bar{\alpha}_1^0 \quad (35)$$

In Eq. (35), $\bar{C}_T$ is steady thrust, $\bar{\alpha}_1^0$ is the steady uniform induced flow, and $V_T = \sqrt{\mu^2 + \lambda^2}$. The wake model can then be considered as a model for perturbation pressure and velocity about this steady, uniform pressure

$$\bar{\tau}_1^{0c} = \frac{\sqrt{3}}{2}\bar{C}_T \quad (36)$$

Following Ref. 14, a completely nonlinear version of Eqs. (23) and (24) can also be obtained if we

1) take V as V_T in the first column ($r = 0$) of $[\bar{L}^c]^{-1}$, but as V for $r \ne 0$.
2) treat all quantities as total rather than perturbation.
3) replace the static λ_m, Eq. (35), by the unsteady value, $\sqrt{3}\alpha_1^0$.

This makes the theory nonlinear, in that V and V_T will depend upon the states, α_n^m. The nonlinear version is used in the correlations in this paper.

Generalized Forces

In order for the model to be coupled with blade lift theory, the τ_n^{mc} and τ_n^{ms} need to be appropriately related to the blade lift. If we treat the pressure across the disk as a lifting line for each blade, rotating with angular velocity Ω, then the azimuth of the q^{th} lifting line (i.e., blade) is $\psi_q = \Omega t + (q - 1)2\pi/Q$. These rotating pressure spikes can then be expanded as in Eq. (9) to obtain the pressure harmonics, Ref. 12.

$$\tau_n^{0c} = \frac{1}{2\pi}\sum_{q=1}^{Q}\left[\int_0^1 \frac{L_q}{\rho\Omega^2 R^3}\phi_n^m(\bar{r})d\bar{r}\right] \quad (37)$$

$$\tau_n^{mc} = \frac{1}{\pi}\sum_{q=1}^{Q}\left[\int_0^1 \frac{L_q}{\rho\Omega^2R^3}\,\phi_n^m(\bar{r})d\bar{r}\right]\cos(m\psi_q) \quad (38)$$

$$\tau_n^{ms} = \frac{1}{\pi}\sum_{q=1}^{Q}\left[\int_0^1 \frac{L_q}{\rho\Omega^2R^3}\,\phi_n^m(\bar{r})d\bar{r}\right]\sin(m\psi_q) \quad (39)$$

where L_q is blade sectional circulatory lift that can be evaluated from a lift theory. Since the wake and lift are now treated separately, the lift theory need not be linear. It can include dynamic stall or other nonlinear effects. Although the above integrals assume that the lift is concentrated along a lifting line at ψ_q, Ref. 12 shows that the integrals are easily modified to include lift distributed over a chordwise surface. Note also that the τ_n^m take on the character of generalized forces. Thus, we have a complete, three-dimensional unsteady wake model written in terms of a finite number of states α_j' and β_j'.

Computation of Induced Flow

The generalized dynamic wake equations have been applied to the prediction of dynamic response of the flow field associated with an isolated rotor in forward flight. The computation of induced inflow at the rotor disk consists of solving the system of Eqs. (23) and (24), simultaneously. In order to do this, the forcing functions on the right-hand side of the equations (*i.e.*, τ_n^{mc}, and τ_n^{ms}) need to be evaluated from Eqs. (37)–(39). Therefore, in addition to the basic dynamic wake equations, we will proceed to establish the expressions for lift.

Blade Lift Model

For this induced inflow computation, we have made the following main assumptions: 1) reversed flow neglected, 2) blade angle of attack is assumed small, 3) there is no blade dynamics, 4) there is no interaction between fuselage and rotor aerodynamics, and 5) the reduced frequency is small enough that $\dot{\theta}$ and $\ddot{\theta}$ terms can be neglected.

Based on these assumptions, the blade sectional lift can be written as

$$\frac{L_q(\bar{r},\psi_q,\bar{t})}{\rho\Omega^2R^3} = \frac{1}{2}a\bar{c}(\bar{r}+\mu\sin\psi_q)^2\left\{\theta_q - \frac{[w(\bar{r},\psi_q,\bar{t})+\lambda_f]}{(\bar{r}+\mu\sin\psi_q)}\right\} \quad (40)$$

where θ_q, the q^{th} blade pitch angle, is

$$\theta_q = \theta_0 - \theta_t\bar{r} + \theta_{1c}\cos\psi_q + \theta_{1s}\sin\psi_q \quad (41)$$

and w is the induced inflow as given in Eq. (21). It is noted that the induced inflow, w, enters the blade lift expression and couples the sine and cosine parts of the dynamic wake equations. Substitution of the blade lift, Eq. (40), into Eqs. (37)–(39) yields generalized-force integrals, (τ_n^{0c}, τ_n^{mc}, and τ_n^{ms}). Although Eq. (40) appears to be a two-dimensional quasi-steady model, the inflow feedback through w implies that both the unsteady effects (e.g., Theodorsen and Loewy) and tip relief effects (*e.g.*, Prandtl and Goldstein tip-loss) are included implicitly.

Solution Method

The resultant set of coupled inflow and lift equations is a system of ordinary differential equations with periodic coefficients. These can be solved by a variety of methods including harmonic balance or direct time-marching. In either event, one must also find the trim settings to give a desired thrust coefficient and desired roll and pitch moments. In our model, $\bar{C}_T = (2/\sqrt{3})\bar{\tau}_1^{0c}$; and roll and pitch moments are proportional to τ_2^{1c} and τ_2^{1s}. This makes trimming a straightforward process. In the work here, we use time-marching with the auto-pilot system described in Ref. 15. For a typical problem with 33 flow states, the method requires 2 minutes CPU on a CDC 855. About half of this is to find trim. This CPU time is much faster than either free-wake programs or prescribed-wake codes.

The choice of inflow states is based on the relationships in Table 1. The table shows the number of radial shape functions for each harmonic (m) in order to have radial terms up to a given power of $\bar{r}$. For example, for terms up to $\bar{r}^4$, the $m = 0$ harmonic would have three radial terms; the $m = 1$ and $m = 2$ sine and cosine harmonics would have 2 terms each; and the $m = 3$ and $m = 4$ sine and cosine harmonics would have one term each. Thus, a total of 15 terms (or state variables) would be used. If we desire more polynomials without increasing the total number of harmonics, we choose a row corresponding to a larger power of $\bar{r}$. For example, for $m = 4$ and $\bar{r}^8$, this would be $5 + 2(4 + 4 + 3 + 3) = 33$ total states, S.

Experimental Data

All of the experimental data used in this paper are from the LDV measurements made by the Army Labs at NASA Langley, Ref. 16. There are two different blade planforms for which data are available. One set of blades has 13° of linear twist, a uniform chord over the inner 75 percent radius, and a 3-to-1 blade taper over the outer 25 percent. The other blades have 8° of linear twist and are constant-chord. Each set has a 25 percent root cutout, a solidity of 0.0977, and was tested as a 4-bladed configuration at $\bar{C}_T = .0064$. Results for the tapered blades are available at $\mu = .15$ and $\mu = .23$. Results for the rectangular blades are available at these two advance ratios and at $\mu = 0.3$. Data at the lower advance ratios are for 3° nose down shaft angle, and data at $\mu = 0.3$ are for 4° nose down shaft angle. The measurements are taken one chord above the tip-path plane in contrast to our calculations, which are at the rotor plane. All results have cyclic flapping trimmed to zero.

The experimental data also include values of the trimmed pitch settings for each data condition. We have compared these with the trimmed pitch settings from our auto-pilot. The average difference in settings for the tapered blades is 0.5°, and the average difference for rectangular blades is 1.1°. From our model, the 3/4 radius trim settings are nearly identical for the two sets of blades.

Contour Plots for Tapered Blades

Figure 1a gives computed induced flow contours with four harmonics and with 15 state-variables at $\mu = 0.15$. Figure 1b gives the measured values at the same condition. One can see that the computation with 15 state variables gives a good representation of all flow characteristics including: 1) The existence of upwash at the front of the disk, 2) the "double-S" shape of the $w = .02$, .03, and .04 contours around the $w =$

Table 1 Number of Shape Functions per Harmonic

Highest Power of $\bar{r}$	Harmonic Number, m									Total Inflow States
	0	1	2	3	4	5	6	7	8	
0	1									1
1	1	1								3
2	2	1	1							6
3	2	2	1	1						10
4	3	2	2	1	1					15
5	3	3	2	2	1	1				21
6	4	3	3	2	2	1	1			28
7	4	4	3	3	2	2	1	1		36
8	5	4	4	3	3	2	2	1	1	45

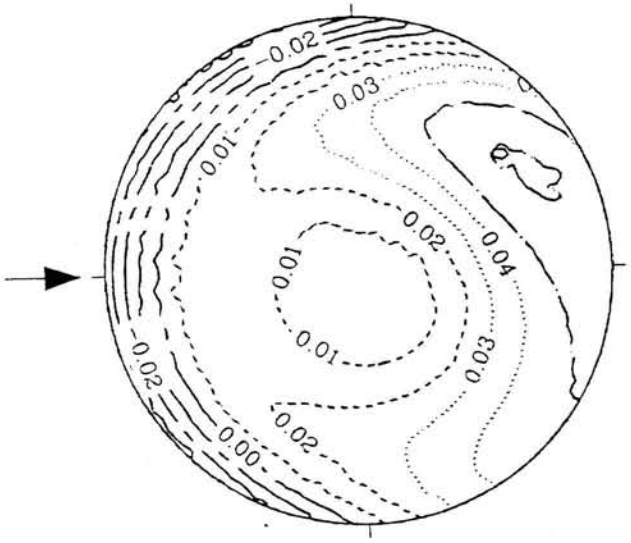

Figure 1a Theoretical induced flow distribution, tapered blades, μ = 0.15, M = 4, S = 15.

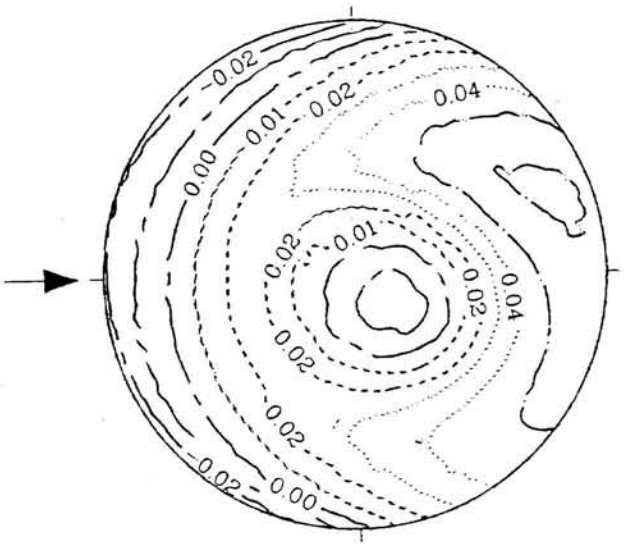

Figure 1c Theoretical induced flow distribution, tapered blades, μ = 0.15, M = 4, S = 33.

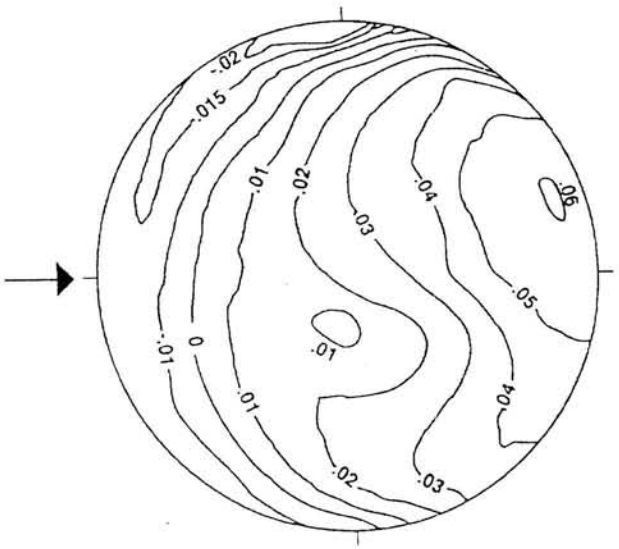

Figure 1b Experimental induced flow distribution, tapered blades, μ = 0.15.

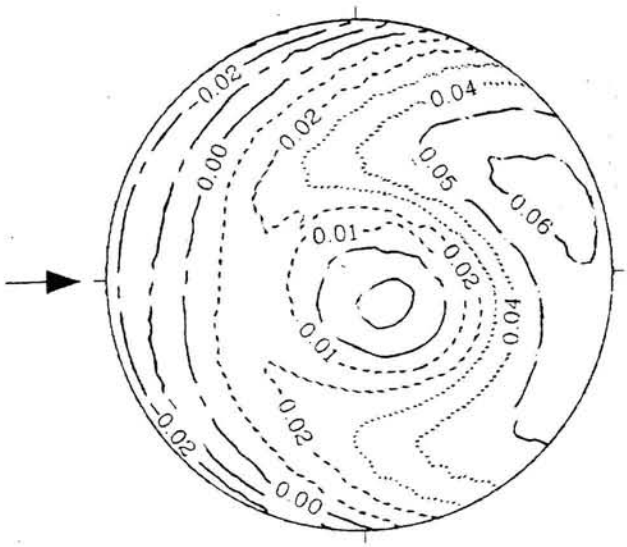

Figure 1d Theoretical induced flow distribution, tapered blades with fuselage, μ = 0.15, M = 4, S = 33.

.01 contour on the retreating side, and 3) the skewing of induced flow toward the advancing side with a maximum of w = 0.06 at ψ = 30°, $\bar{r}$ = 0.85. One discrepancy, however, is the overly large gradient in computed induced flow at ψ = 180°. This discrepancy is alleviated, however, when (with M = 4) we increase to 33 state variables, Fig. 1c. The correlation becomes better yet when we add the flow over the fuselage from Ref. 17, Fig. 1d. A similarly good correlation is seen for μ = 0.23 when we include 33 states and fuselage flow, Figs. 2a–2b.

We have seen in Fig. 1 that the flow over the fuselage gives a marked improvement in data correlation. Figures 3 and 4 show the effect of fuselage flow in more detail. In these figures, we plot induced flow with and without fuselage flow both on the longitudinal centerline (ψ = 0°, 180°) and on the lateral center line (ψ = 90°, 270°) at μ = 0.15 and 0.23. Results show no effect of the fuselage on the flow at the lateral centerline, but they show a noticeable improvement in correlation on the longitudinal centerline. This improvement is more significant at μ = 0.23 due to the larger relative freestream. Therefore, flow over the fuselage is included in all results to follow.

Convergence of Method

We have seen in Figs. 1a–1c that the correlation at μ = 0.15 improves at the leading edge of the disk if more inflow states are added. To study this effect further, we now investigate in detail the influence of the number of states on the convergence and correlation. Figure 5 shows the identical centerline results as in Fig. 4 (μ = 0.23 with flow over the fuselage), but the number of states is increased from 15 ($\bar{r}^4$ terms) to 33 ($\bar{r}^8$ terms). Convergence to the measured values at the leading edge is clearly seen from comparison of Figs. 4 and 5. Figure 6 details this convergence for μ = 0.15. Figure 6a gives results at ψ = 180°, the leading edge, where we saw the greatest effect in Fig. 1. The three results are for 15, 33, and 51 state variables, respectively. It is clear from the curves that the

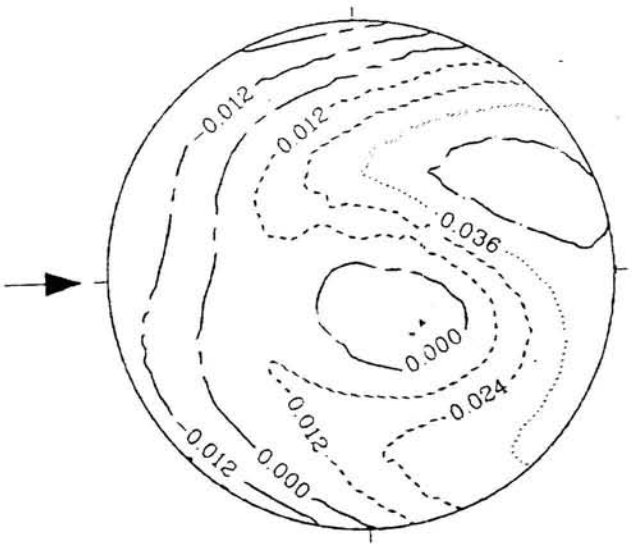

Figure 2a Theoretical induced flow distribution, tapered blades with fuselage, $\mu = 0.23$, $M = 4$, $S = 33$.

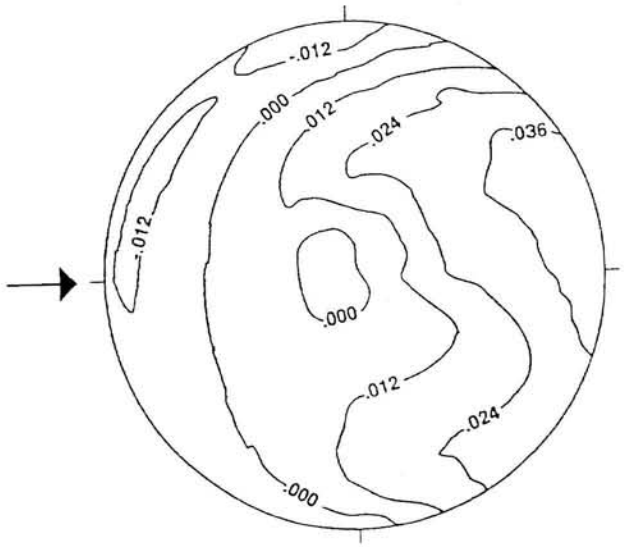

Figure 2b Experimental induced flow distribution, tapered blades, $\mu = 0.23$.

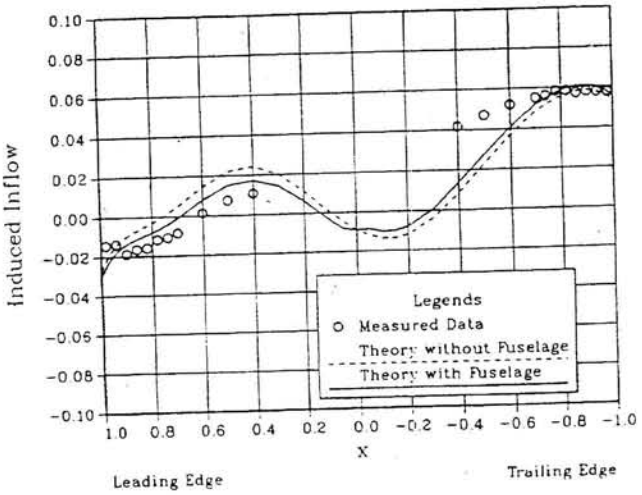

Figure 3a Longitudinal variation of induced flow, tapered blades, $\mu = 0.15$, $M = 4$, $S = 33$.

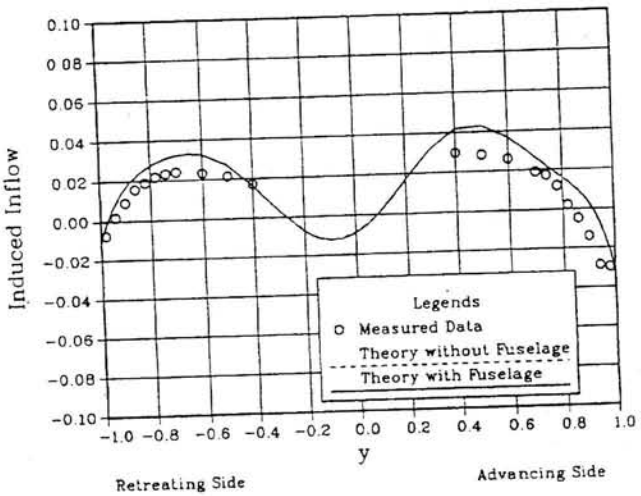

Figure 3b Lateral variation of induced flow, tapered blades, $\mu = 0.15$, $M = 4$, $S = 33$.

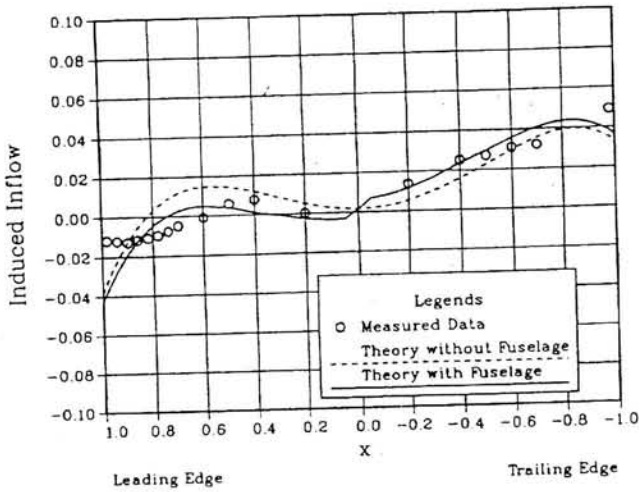

Figure 4a Longitudinal variation of induced flow, tapered blades, $\mu = 0.23$, $M = 4$, $S = 15$.

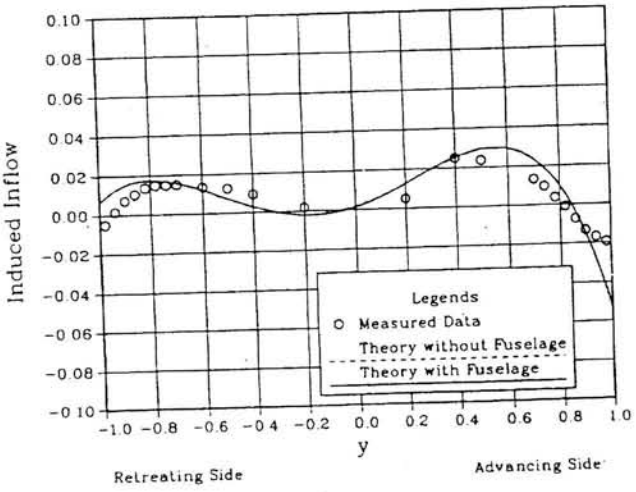

Figure 4b Lateral variation of induced flow, tapered blades, $\mu = 0.23$, $M = 4$, $S = 15$.

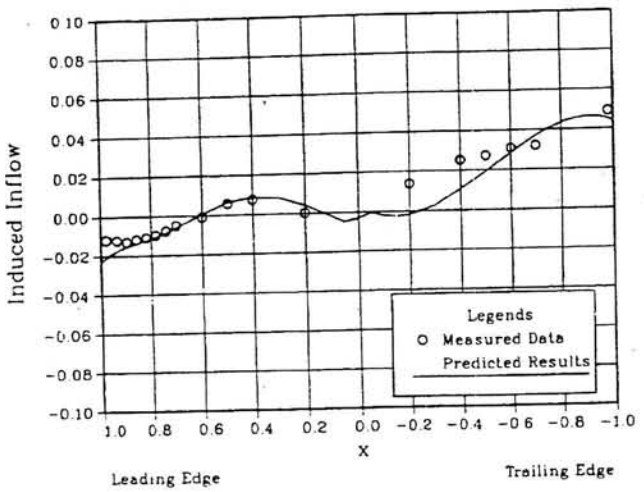

Figure 5a Longitudinal variation of induced flow, tapered blades with fuselage, $\mu = 0.23$, $M = 4$, $S = 33$.

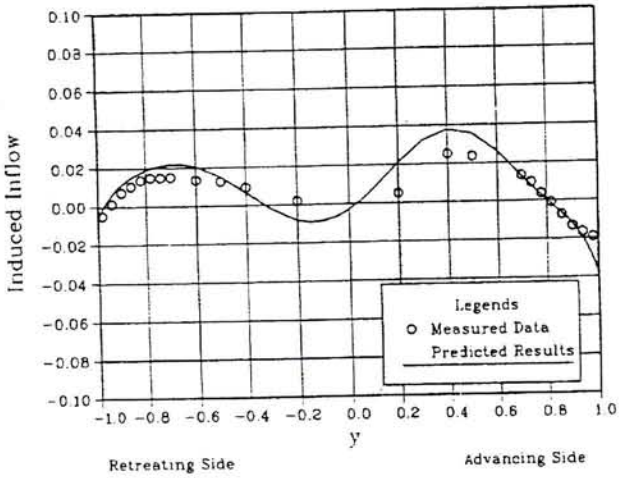

Figure 5b Lateral variation of induced flow, tapered blades with fuselage, $\mu = 0.23$, $M = 4$, $S = 33$.

computed flow at the rotor edge is converging to an answer very close to the measured flow. The results with $S = 15$ show an excessive inflow gradient near $\bar{r} = 1$, whereas results for $S = 33$ and $S = 51$ are moving toward the data and have a "flat" distribution for $0.8 < \bar{r} < 1.0$. Figures 6b and 6c show the same comparison for $\psi = 0°$ and $\psi = 30°$ (the latter being the azimuth of maximum induced flow). In these cases, the flow at the trailing edge has already converged; but the flow in the center of the disk is changing with S, due to convergence on the effect of the root vortex. Interestingly, the data at $\psi = 0°$ do not seem to agree with the calculations at $\bar{r} < 0.4$, while those at $\psi = 30°$ do. We believe that the hub and fuselage-wake interaction may account for the discrepancy at $\psi = 0°$, $\bar{r} < 0.4$.

In general, 15 state variables capture the major flow effects, but 33 states capture more detail at the rotor edge. We have also computed inflow with 8 and 12 harmonics, respectively. There is no appreciable change in time-averaged inflow. Therefore, $M = 4$ is sufficient for the tapered blades.

Comparison with other Methods

Although our model is not designed as a detailed performance model, it is interesting to compare it with other, more performance-oriented models. Figure 7 shows contour plots for the tapered blade at $\mu = 0.15$ from free-wake and prescribed-wake models, Ref. 18 (neither of these results includes flow over the fuselage). These can be compared with the data and with our computations in Fig. 1. We see that the present model is as good or better than these other methodologies, despite its simpler assumptions. For example, the current model predicts

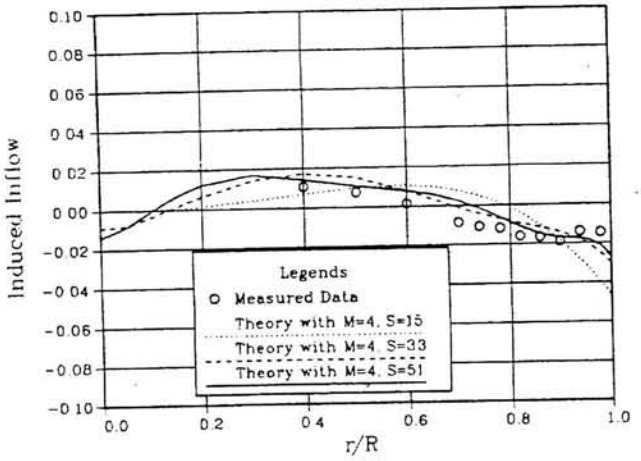

Figure 6a Effect of number of shape functions on time-averaged induced flow modeling, tapered blades with fuselage, $\mu = 0.15$, $\psi = 180°$.

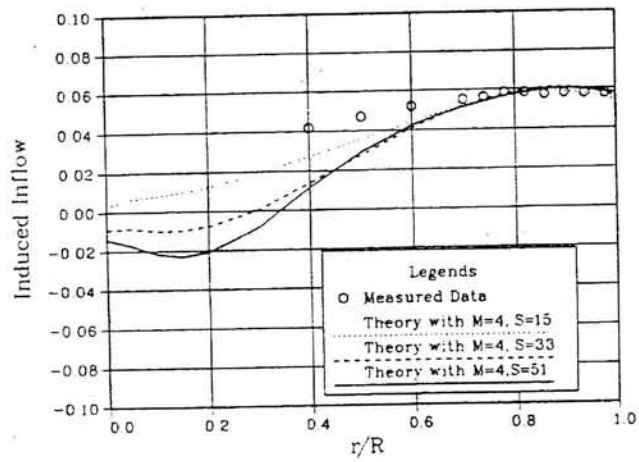

Figure 6b Effect of number of shape functions on time-averaged induced flow modeling, tapered blades with fuselage, $\mu = 0.15$, $\psi = 0.0°$.

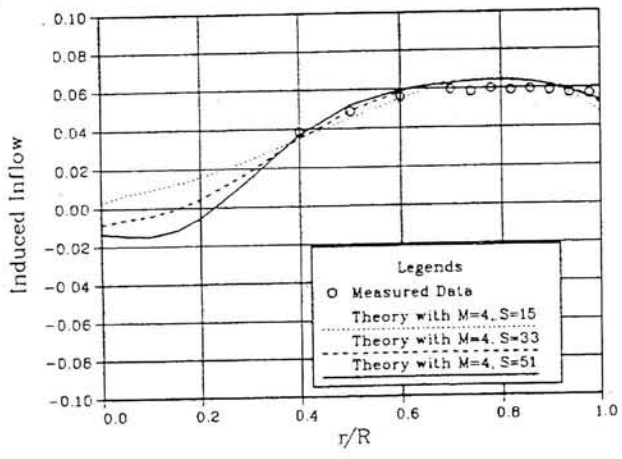

Figure 6c Effect of number of shape functions on time-averaged induced flow modeling, tapered blades with fuselage, $\mu = 0.15$, $\psi = 30.0°$.

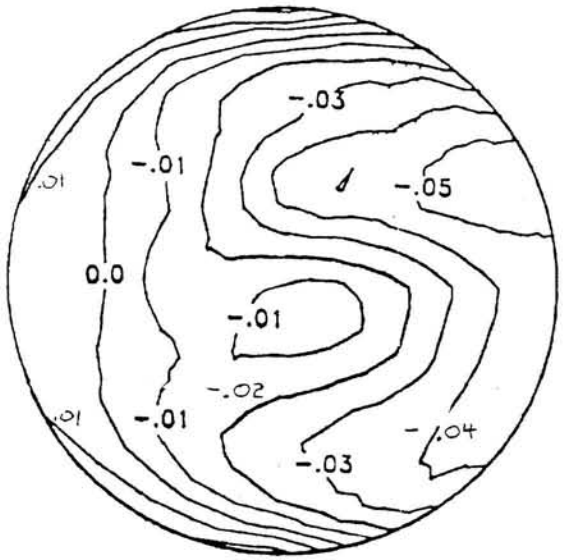

Figure 7a Computed induced flow distribution, prescribed wake, tapered blades, $\mu = 0.15$.

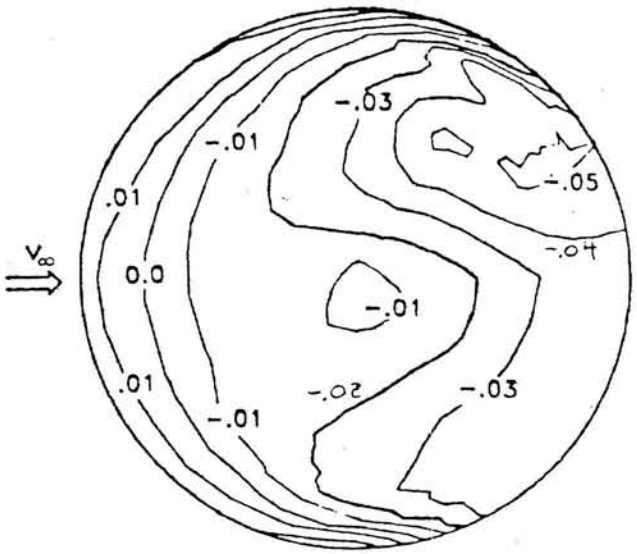

Figure 7b Computed induced flow distribution, free wake, tapered blades, $\mu = 0.15$.

the maximum measured contour of 0.06, whereas the methodologies in Fig. 7 do not. A possible explanation for this better correlation is that, although our model lacks wake distortion and wake roll-up, it has no discretization errors. In other words, the wake is continuous along the blade span and is shed continuously behind the blade rather than being modeled by a few vortex panels. Thus, for some problems (especially nearly flat wakes as we have for this data set), our model may sometimes out-perform other wake models due to reduced computational approximations.

Rectangular Blades

We now turn to correlation with the data for rectangular blades. Figures 8a–f compare theoretical and experimental contour plots at $\mu = 0.15$, 0.23, and 0.30. The theoretical results are for $S = 33$ and include flow over the fuselage. In general, the theory shows good agreement with the major flow features, but the correlations are not as good as for the tapered blades. This discrepancy at the tip can be seen more clearly in results along the lateral and longitudinal axes, Figs. 9a–f. Figures 9a–b show small errors in the tip regions near $\bar{r} = 1$, similar to the unconverged results in Fig. 4. However, the correlation at the center is better than in Fig. 4. The overall correlation deteriorates at $\mu = 0.23$, Figs. 9c–d, and at $\mu = 0.30$. Figs. 9e–f. We have also done this computation with up to 51 states. Correlation improves at the tips, but is still not completely accurate.

The difference in convergence between rectangular blades and tapered blades is due to the fact that rectangular blades with 8° of twist have less lift inboard and more lift outboard than do the tapered blades with 13° twist. Thus, the tapered blades have a stronger root vortex (slowing convergence in the center), while the rectangular blades have a stronger tip vortex (slowing convergence at the blade tips).

Although the above correlation is not as good as it was for the tapered blades, the accuracy must be placed in perspective. Reference 19 provides a comparison of these data with five other wake models. A comparison of our results with those in

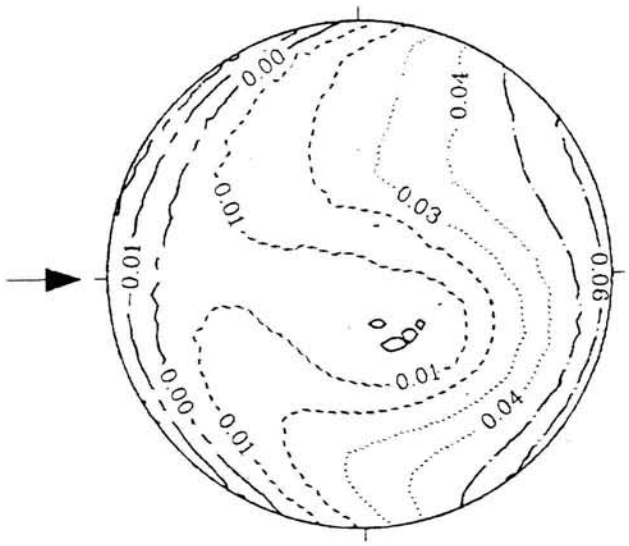

Figure 8a Theoretical induced flow distribution, rectangular blades with fuselage, $\mu = 0.15$, $M = 4$, $S = 33$.

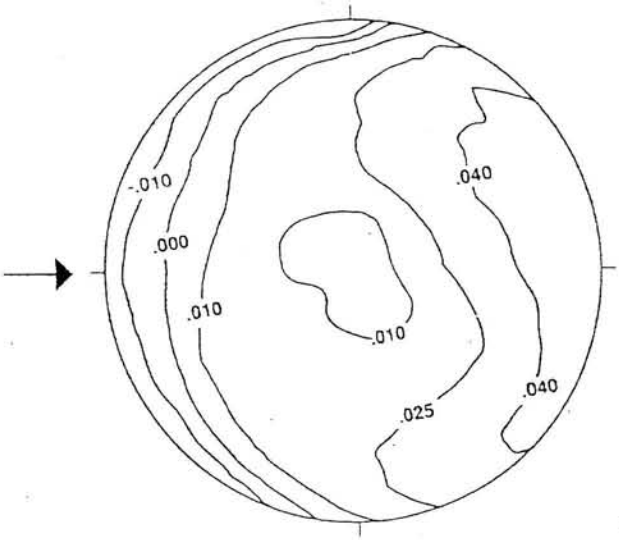

Figure 8b Experimental induced flow distribution, rectangular blades, $\mu = 0.15$.

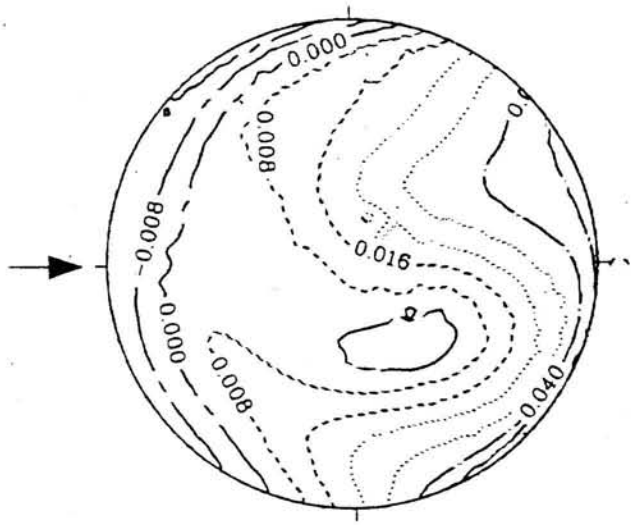

Figure 8c Theoretical induced flow distribution, rectangular blades with fuselage, $\mu = 0.23$, $M = 4$, $S = 33$.

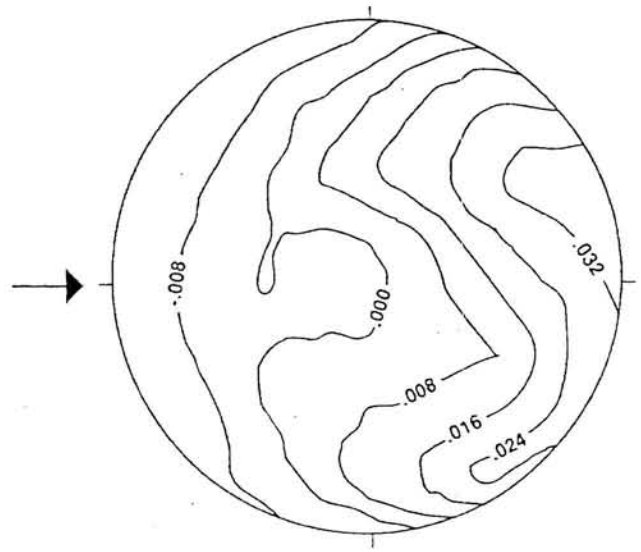

Figure 8d Experimental induced flow distribution, rectangular blades, $\mu = 0.23$.

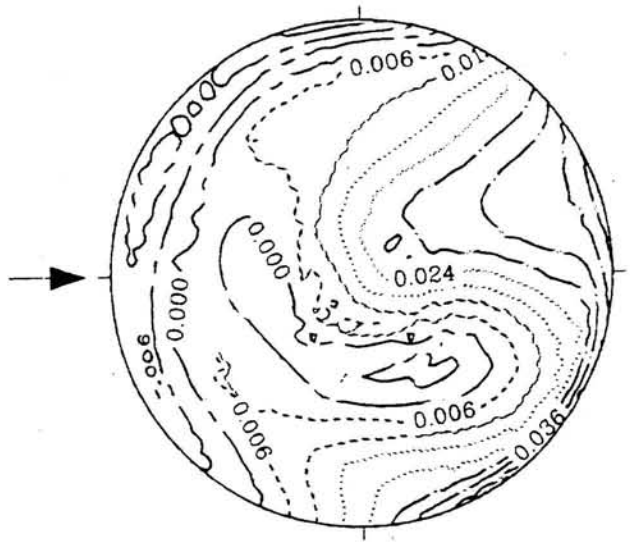

Figure 8e Theoretical induced flow distribution, rectangular blades with fuselage, $\mu = 0.30$, $M = 4$, $S = 33$.

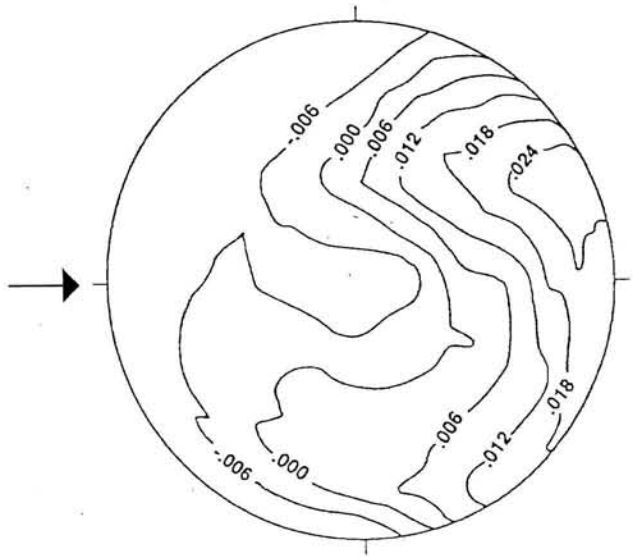

Figure 8f Experimental induced flow distribution, rectangular blades, $\mu = 0.30$.

Ref. 19 shows that, despite the slow convergence, the present model with $S = 33$ does as well or better than the other models tested.

An important point is that, despite the fact that our model does well for tapered blades (and fairly well for rectangular blades), a detailed induced flow computation is not the end product of this theory. The utility of our model comes from the need to perturb the wake about this steady-state solution. It is these aeroelastic perturbation equations that are best formulated with our finite-state model. Thus, we do not need to be completely accurate on induced flow or even on lift. We do need to be accurate on the generalized lifting forces associated with wake perturbation. Thus, modeling of flow details is much less important for aeroelasticity than it is for performance.

Summary and Conclusions

An unsteady, three-dimensional induced-flow model has been successfully applied to the computation of the induced-flow distribution of a rotor in forward flight, and numerical results have been compared against LDV measurements for induced flow at the disk. The major conclusions of this comparison are given below. However, these must be tempered by the facts that the comparisons are only for two particular blade planforms at three advance ratios, and that results are obtained only for two shaft angles, one value of $\overline{C}_T$, and one solidity.

1. The time-averaged induced flow from this method gives good correlation with measured data with the exception of just behind the pylon at the lowest advance ratio, and near the blade tips for rectangular blades at high advance ratios.

2. The method performs as well as or better than other codes that have been applied to this data; but the new method takes less computing time, and it is better suited for aeroelastic analysis.

3. Results with only 4 harmonics and 15 state variables converge to all fundamental characteristics of the time-averaged flow. However, for accurate flow near blade tips (especially at $\psi = 180°$), we require 33 state variables for tapered blades and more than 51 states for the rectangular blades.

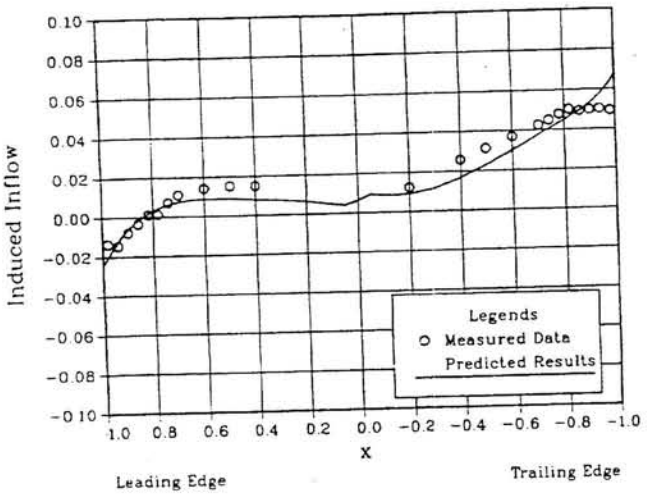

Figure 9a Longitudinal variation of induced flow, rectangular blades with fuselage, $\mu = 0.15$, $M = 4$, $S = 33$.

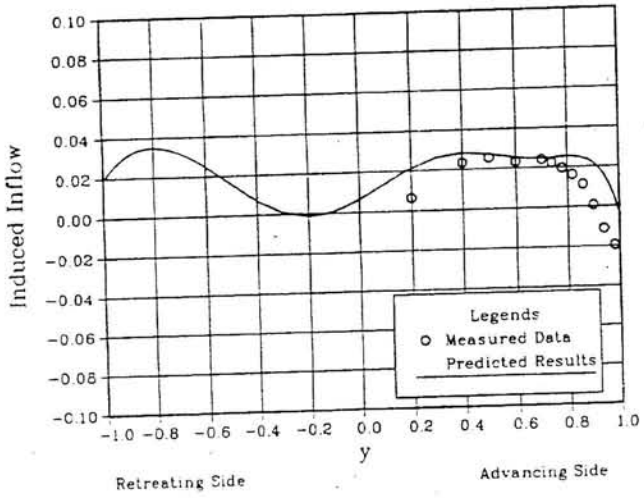

Figure 9b Lateral variation of induced flow, rectangular blades with fuselage, $\mu = 0.15$, $M = 4$, $S = 33$.

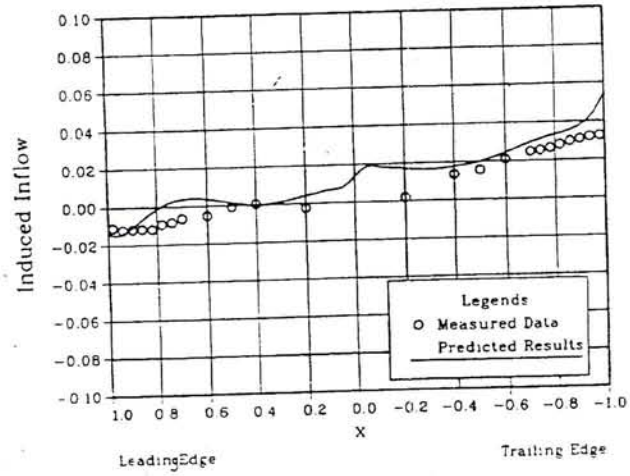

Figure 9c Longitudinal variation of induced flow, rectangular blades with fuselage, $\mu = 0.23$, $M = 4$, $S = 33$.

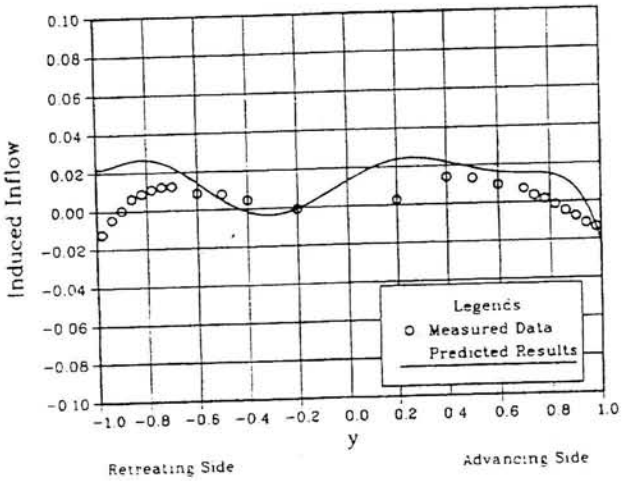

Figure 9d Lateral variation of induced flow, rectangular blades with fuselage, $\mu = 0.23$, $M = 4$, $S = 33$.

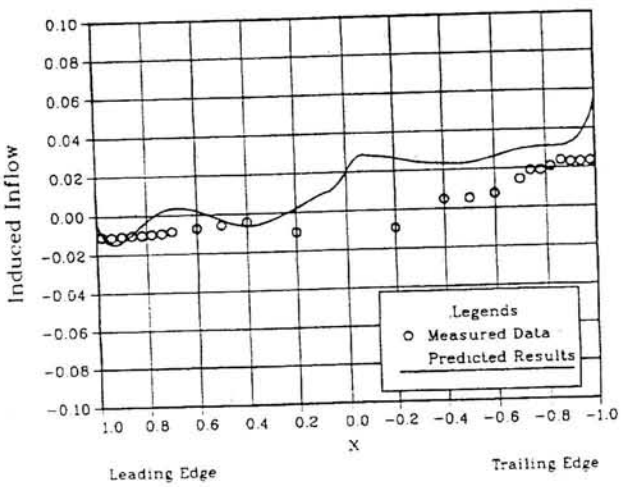

Figure 9e Longitudinal variation of induced flow, rectangular blades with fuselage, $\mu = 0.30$, $M = 4$, $S = 33$.

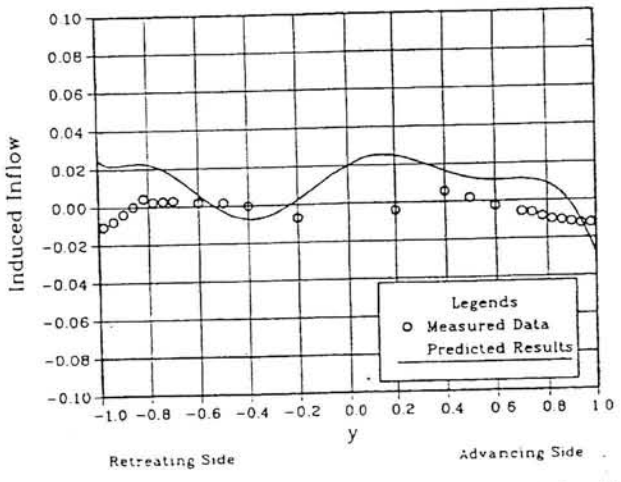

Figure 9f Lateral variation of induced flow, rectangular blades with fuselage, $\mu = 0.30$, $M = 4$, $S = 33$.

4. For accurate correlation, one needs the flow over the fuselage to be included in the analysis.

Acknowledgment

This work was sponsored by a joint NASA-Army grant, NAG-2-462, Bob Ormiston, Bill Warmbrodt, and Benton Lau technical monitors. Additional funding was provided by the Georgia Tech Center of Excellence for Rotary Wing Aircraft Technology, sponsored by the Army Research Office.

References

[1]Loewy, R. G., "A Two Dimensional Approach to the Unsteady Aerodynamics of Rotary Wings," *Journal of the Aeronautical Sciences*, Vol. 24, (2), Feb 1957.

[2]Friedmann, P. P., and Venkatesan, C., "Finite State Modeling of Unsteady Aerodynamics and Its Application to a Rotor Dynamic Problem," 11th European Rotorcraft Forum, London, Sep 1985.

[3]Mangler, K. W., "Calculation of the Induced Velocity Field of a Rotor," Royal Aircraft Establishment, Report No. Aero 2247, Sep 1948.

[4]Heyson, H. H., and Kotzoff, S., "Induced Velocities Near a Lifting Rotor with Nonuniform Disk Loading," NASA TR 1319, 1957.

[5]Wang, Shi-Cun, "Generalized Rotor Vortex Theory, Problems of Helicopter Rotor Aerodynamics," U.S.S.R., 1961 (see also, Mil, M. J., *Helicopters, Calculation and Design*, NASA TT F-494, Sep 1967).

[6]Miller, R. H., "Rotor Blade Harmonic Air Loading," *AIAA Journal*, Vol. 2, (7), Jul 1964.

[7]Scully, M. P., "A Method of Computing Helicopter Vortex Wake Distortion," MIT, ASRL TR138-1, Jun 1967.

[8]Landgrebe, A. J., "An Analytical Method for Predicting Rotor Wake Geometry," *Journal of the American Helicopter Society*, Vol. 14, (4), Oct 1969.

[9]Sadler, S. G., "Development and Application of a Method for Predicting Rotor Free Wake Positions and Resulting Blade Airloads," NASA CR-1911 Vol. I: Model and Results, NASA CR-1912 Program Listing, 1971.

[10]Runyan, Harry L., and Tai, Hsiang, "Application of a Lifting Surface Theory for a Helicopter in Forward Flight," 11th European Rotorcraft Forum, London, Sep 1985.

[11]Pitt, D. M., and Peters, D. A., "Theoretical Prediction of Dynamic Inflow Derivatives," *Vertica*, Vol. 5, (1), Mar 1981.

[12]Peters, D. A., Boyd, D. D., and He, Chengjian, "Finite-State Induced-Flow Model for Rotors in Hover and Forward Flight," *Journal of the American Helicopter Society*, Vol. 34, (4), Oct 1989.

[13]He, Chengjian, *Development and Application of a Generalized Dynamic Wake Theory for Lifting Rotors*, Ph.D. Thesis, School of Aerospace Engineering, Georgia Institute of Technology, Jul 1989.

[14]Peters, D. A., and Ninh HaQuang, "Dynamic Inflow for Practical Application," *Journal of the American Helicopter Society*, Vol. 33, (4), Oct 1988.

[15]Peters, D. A., Kim, B. S., and Chen, H. S., "Calculation of Trim Settings for a Helicopter Rotor by an Optimized Controller," *Journal of Guidance, Control and Dynamics*, Vol. 7, (1), Jan–Feb 1984.

[16]Elliott, J. W., and Althoff, S. L., "Inflow Measurement Made with a Laser Velocimeter on a Helicopter Model in Forward Flight," Vols. I–V, NASA TM's 100541-100545, Apr 1988.

[17]Berry, John D., and Althoff, Susan L., "Computing Induced Velocity Perturbations due to a Helicopter Fuselage in a Freestream," NASA TM 4113, Jun 1989.

[18]Berry, J. D., Hoad, D. R., Elliott, J. W., and Althoff, S. L., "Helicopter Rotor Induced Velocities-Theory and Experiment," AHS National Specialists' Meeting on Aerodynamics, and Aeroacoustics, Arlington, Tex., Feb 1987.

[19]Hoad, Danny R., Althoff, Susan, L., and Elliott, J. W., "Rotor Inflow Variability with Advance Ratio," American Helicopter Society 44th Annual Forum, Washington, D.C., Jun 1988.